Flow Turbulence Combust (2011) 86:63–88
DOI 10.1007/s10494-010-9287-y

Swirling and Impinging Effects in an Annular Nonpremixed Jet Flame

Xi Jiang · K. H. Luo · L. P. H. de Goey · R. J. M. Bastiaans · J. A. van Oijen

Received: 18 October 2009 / Accepted: 14 July 2010 / Published online: 30 July 2010

Abstract The effects of swirl and downstream wall confinement on an annular nonpremixed flame were investigated using direct numerical simulation (DNS). Fully three-dimensional parallel DNS was performed employing high-order numerical methods and high-fidelity boundary conditions to solve governing equations for variable-density flow and finite-rate Arrhenius chemistry. Three swirl numbers have been examined: 0 (without swirl), 0.4 and 0.8, while the effects of downstream wall confinement have been examined for swirl numbers 0 and 0.4. Results have been presented in terms of instantaneous and time-averaged flow quantities, which have also been analysed using energy spectra and proper orthogonal decomposition (POD). Effects of swirl on the fluid dynamic behaviour of the annular nonpremixed flame were found to be significant. The fluid dynamic behaviour of the flame is greatly affected by the interaction between the geometrical recirculation zone (GRZ) near the jet nozzle exit due to the annular configuration, the central recirculation zone (CRZ) associated with swirl, the unsteady vortical structures in the jet column due to the shear instability, and the downstream wall confinement. Depending on the degree of swirl, the GRZ near the burner mouth and the CRZ may co-exist or one zone may be overwhelmed by another. At a moderate swirl number, the co-existence leads to a flame with strong reaction attached to the burner mouth; while at a high swirl number, the CRZ dominates over the GRZ. The precessing vortex core was

X. Jiang (✉)
Engineering Department, Lancaster University,
Lancaster LA1 4YR, UK
e-mail: x.jiang@lancaster.ac.uk

K. H. Luo
School of Engineering Sciences, University of Southampton,
Southampton SO17 1BJ, UK

L. P. H. de Goey · R. J. M. Bastiaans · J. A. van Oijen
Department of Mechanical Engineering, Technische Universiteit Eindhoven,
Den Dolech 2, 5600 MB Eindhoven, The Netherlands

observed to exist in the swirling flow fields. The Nusselt number distribution of the annular impinging flames differs from that of round impinging jets. The POD analysis revealed that wall effects on the flow field are mainly associated with the higher mode numbers.

Keywords Swirl · Impinging · Nonpremixed flame · Direct numerical simulation

1 Introduction

Swirling flows are encountered in applications such as internal combustion engines, turbine combustors, furnaces, and boilers. Swirling motion is regarded as an efficient way to stabilize nonpremixed flames and has been used together with bluff-body stabilization, e.g. [1–3]. In such a configuration, a large recirculation zone with flow reversal may be formed in the core region, which carries the combustion products back towards the burner mouth, providing a continuous and stable source of energy for flame ignition. In addition, swirl extends the curved shear layer and produces extra shear promoting turbulence generation that enhances mixing and combustion intensity. In many practical applications, it is preferable to have relatively strong swirl so that there is a formation of pronounced coherent structures involving both axisymmetric and azimuthal vorticity. In combustion applications, coherent vortical structures play an important role as they influence distribution of heat and species to a large extent and hence the entire reaction process.

It is inappropriate to study swirling flows using the traditional Reynolds-averaged Navier-Stokes (RANS) modeling methods due to the existence of unsteady coherent structures and the effects of mean flow streamline curvature [4]. Recently, there has been a substantial amount of large-eddy simulation (LES) of swirling flames, e.g. [5–9], to name but a few. In most of these studies, the swirling flame was established on a round nozzle. For flows established on a round nozzle, there is a circular velocity shear layer near the nozzle exit where flow instability may develop into vortical structures and turbulence downstream. Different from a round nozzle, an annular nozzle has two adjacent velocity shear layers, which may enhance the turbulence level, improve mixing and combustion and reduce pollutant emissions. The burner surface of the annular fuel jet also provides a means of bluff body flame stabilization [10].

Flames in annular configurations are used in industrial and domestic burners such as the cooking flames. For an annular jet, the fluid dynamics is largely determined by the interaction of two adjacent annular shear layers [11]. The prominent features of annular jet flames include the formation of a recirculation zone inside the jet core near the nozzle exit, which can not only enhance the fuel/air mixing but also stabilize the flame. Vanoverberghe et al. [12] experimentally investigated a swirl-stabilized partially premixed combustion in an annular configuration in a confined environment, where different flame states were observed. On the computational side, LES has been used to simulate annular non-reacting swirling jets, e.g. [13, 14]. The LES captured the precessing vortex cores (PVC) which are the inner structures in swirling jets, featuring the vortex core rotating and vortex spinning. However, LES

or DNS of flames in annular configurations under swirling conditions has not been available.

The dynamics of annular swirling flames involves the interaction between the recirculation zone near the nozzle exit, the unsteady vortical structures due to the shear instability, and the CRZ and PVC associated with swirl. The interaction has not been fully understood, which can be affected by the degree of swirl that directly affects the CRZ and PVC. Swirl can enhance turbulence within a flame that is often desirable to achieve, either to improve mixing and to attain well-stirred conditions to reduce NO_x emissions, or to improve the flame stability. However, flames subject to weak swirl and very strong swirl may lead to unstable flames that are not desirable [15]. From a practical point of view, swirl number is an important parameter to control the flame dynamics.

The near-wall combustion is another important topic that deserves more research efforts from both application and fundamental points of view. In this context, the study of impinging jet flames is of particular interest. In addition to the relevance to many engineering applications such as industrial burners, metal cutting, glass shaping, and glass melting for fibre optics production, impinging jet flames are also of great value in fundamental studies. The impinging flow configuration is of simple geometry but covers a broad range of important flow phenomena, such as large- and small-scale structures, wall boundary layers with stagnation, large curvature involving strong shear and normal stresses and wall heat transfer. Impinging flames involve the interactions between the wall and the flame. A variety of combustion modes can be seen in experiments [16], depending on fuel/air mixing and heat transfer, which are strongly influenced by the wall. In a turbulent scenario, the flame/wall/turbulence multi-way interactions bring many unresolved and challenging issues in combustion modelling. In general, near-wall flow and heat transfer in reacting flows are not extensively investigated. The impinging flow contains a broad range of length scales, ranging from the large-scale vortical structure to very thin thermal boundary layers near the wall. The near-wall flow and combustion processes are also highly unsteady. To gain full understanding of turbulent impinging flames needs detailed information on temporally and spatially resolved flow fields, especially in the near-wall regions, which have not been made available using traditional diagnostic and numerical methods.

A full understanding of annular swirling impinging flames needs both temporally and spatially resolved information. By accurately resolving all the relevant time and length scales, DNS provides an effective means to investigate such flames, which can also help developing LES models for such complicated flames. In this study, the dynamics of an annular swirling nonpremixed jet flame has been investigated by performing a three-dimensional (3D) parallel DNS. Highly accurate numerical methods and high-fidelity boundary conditions have been used in the DNS. The code was previously used for DNS of several nonpremixed flames [17–19]. An annular nonpremixed jet flame at different swirl numbers has been investigated. The swirling motion was introduced into the annular fuel jet itself rather than the oxidizer stream [1–3]. In such a configuration, the burner surface area inside the jet annulus provides bluff-body stabilization for the nonpremixed flame. Impinging flames have also been studied to investigate the effects of downstream wall confinement on the flow dynamics.

2 Mathematical Formulation and Numerical Methods

2.1 The physical problem and mathematical formulation

The physical problem considered was a fuel jet issuing into an open boundary domain from an annular nozzle with a swirl applied onto the fuel stream. Combustion took place when the fuel mixed with the oxidant environment. The computational domain was the region above the jet nozzle exit plane. The flow was described with the compressible time-dependent Navier-Stokes equations in the Cartesian coordinate system (x, y, z), where the z-axis is along the streamwise direction of the fuel jet and the $x-0-y$ plane is the domain inlet where the jet nozzle exit locates. The annular jet nozzle is located at $R_i \le r \le R_o$, with $r = \sqrt{x^2+y^2}$ representing the radial distance, R_i and R_o the inner and outer radii of the annular jet respectively. Using the analytical velocity profiles given below, the circular configuration can be represented by the square mesh associated with the Cartesian coordinates employed. The nondimensional form of the governing equations was employed [18]. Major reference quantities used in the normalization were the maximum streamwise mean velocity at the jet nozzle exit (computational domain inlet), nozzle diameter ($R_i + R_o$ measured from the middle points of the annulus), and the ambient temperature, density and viscosity. Since this study was focused on the investigation of the fluid dynamic behaviour of the flame, a simple chemistry $\nu_f M_f + \nu_o M_o \rightarrow \nu_p M_p$ with finite-rate Arrhenius kinetics was considered to be adequate, where M_i and ν_i represent the chemical symbol and stoichiometric coefficient for species i, respectively. The reaction rate, after normalization, takes the form of $\omega_T = Da\left(\rho Y_f/W_f\right)^{\nu_f}\left(\rho Y_o/W_o\right)^{\nu_o}\exp\left[-Ze\left(1/T-1/T_{fl}\right)\right]$, where W and Y represent species molecular weight and mass fraction, and Da, Ze and T_{fl} stand for the Damköhler number, Zeldovich number and flame temperature respectively. The heat release rate in the energy equation was given by $\omega_h = Q_h\omega_T$ with Q_h representing heat of combustion. The governing equations for the reacting flow were supplemented by the ideal-gas law for the mixture [18].

2.2 Boundary conditions

Boundary conditions for the 3D spatial DNS of annular jet flames represent a challenging problem. Physical conditions at the nozzle exit must be appropriately represented. In the meantime, open boundary conditions in the jet cross-streamwise direction should allow jet mixing with the ambient and entrainment. The Navier-Stokes characteristic boundary condition (NSCBC) by Poinsot and Lele [20] was utilized. For the nozzle exit or the computational domain inlet, the NSCBC was used to specify the inflow boundary with density treated as a "soft" variable that fluctuated slightly in the simulations according to the characteristic waves at the boundary. To specify accurately the swirl number in a numerical simulation is also a delicate issue. Based on the assumption of equilibrium swirling inflow, analytical solution was derived for the mean velocity profiles [21], including the mean streamwise velocity $\overline{w}$ and the mean azimuthal velocity $\overline{u}_\theta$

$$\overline{w} = -\frac{1}{4}\frac{f_x}{\mu}\left(r^2 - \frac{R_i^2 - R_o^2}{\ln R_i - \ln R_o}\ln r + \frac{R_i^2 \ln R_o - R_o^2 \ln R_i}{\ln R_i - \ln R_o}\right) \tag{1}$$

$$\overline{u}_\theta = -\frac{1}{3}\frac{f_\theta}{\mu}\left(r^2 - \frac{R_i^2 + R_i R_o + R_o^2}{R_i + R_o}r + \frac{R_i^2 R_o^2}{R_i + R_o}\frac{1}{r}\right) \tag{2}$$

Equations 1 and 2 only hold for the jet annulus $R_i \le r \le R_o$, and zero velocities have been specified outside the jet annulus. The f_x and f_θ in Eqs. 1 and 2 can be defined by the maximum velocities and the degree of swirl at the inflow boundary. For a unit maximum velocity (which is often the case when a non-dimensional form of the governing equations is employed), the constant f_x is defined as

$$f_x = -\frac{8\mu\,(\ln R_o - \ln R_i)}{R_o^2 - R_i^2 + R_i^2 \ln\left[\frac{R_i^2 - R_o^2}{2(\ln R_i - \ln R_o)}\right] - R_o^2 \ln\left[\frac{R_i^2 - R_o^2}{2(\ln R_i - \ln R_o)}\right] - 2\,R_i^2 \ln R_o + 2\,R_o^2 \ln R_i} \tag{3}$$

The parameter f_θ defines the degree of swirl. For known $\overline{w}$ and $\overline{u}_\theta$ the swirl number can be calculated from

$$S = \frac{\int_{R_i}^{R_o} \overline{w}\,\overline{u}_\theta r^2 dr}{R_o \int_{R_i}^{R_o} \overline{w}^2 r dr} \tag{4}$$

A certain swirl number can be conveniently achieved by adjusting the constant f_θ in Eq. 2 for $\overline{u}_\theta$. From the azimuthal velocity $\overline{u}_\theta$, the cross-streamwise velocity components at the inflow can be specified by $\overline{u} = -\overline{u}_\theta\, y/r$ and $\overline{v} = \overline{u}_\theta\, x/r$. In this study, the inlet velocity profiles have been perturbed by small helical disturbances [22, 23]. The velocity components at the jet nozzle exit (computational domain inlet) $z = 0$ were given as

$$u = \overline{u} + A\sum_m \sin\,(m\theta - 2\pi f_0 t) \tag{5}$$

$$v = \overline{v} + A\sum_m \sin\,(m\theta - 2\pi f_0 t) \tag{6}$$

$$w = \overline{w} + A\sum_m \sin\,(m\theta - 2\pi f_0 t) \tag{7}$$

In Eqs. 5–7, A stands for the amplitude of disturbance which was specified as 1% of the maximum value of streamwise mean velocity $\overline{w}$ while m stands for the mode number. The application of external perturbation leads to the formation of vortical structures in the jet column [24]. In the simulations performed, two helical modes of $m = 1$ and $m = -1$ were superimposed on the temporal disturbance. The nondimensional frequency of the unsteady excitation was $f_0 = 0.30$, which was chosen to be the unstable mode leading to the jet preferred mode of instability [25]. The fuel is injected from the annulus with $R_i = 0.4$ and $R_o = 0.6$, while the fuel temperature at the inlet was chosen to be 3 to ensure auto-ignition of the mixture.

The annular jet flame is open to the ambient environment in the cross-streamwise directions. In the streamwise direction, the flow is bounded by the inlet conditions and the downstream wall conditions for the impinging cases, while it is open to the ambient environment for the non-impinging cases. The downstream wall conditions and open-boundary conditions in both the downstream and cross-streamwise directions were specified using NSCBC. The downstream wall has been assumed to

be non-slip for velocities and non-permeable for chemical species and at constant temperature of the ambient environment, therefore the flame may extinguish on the wall surfaces. The open-boundary conditions specified using NSCBC allow the entrainment of the ambient fluids.

2.3 Numerical methods

The numerical methods include high-order finite-difference schemes for time advancement and spatial discretization. The equations were discretized using a sixth-order accurate compact (*Padé*) finite-difference scheme for evaluation of the spatial derivatives [26], which has been extensively used in DNS of fluid flow problems. The finite-difference scheme allows flexibility in the specification of boundary conditions for minimal loss of accuracy relative to spectral methods. The time-dependent governing equations were integrated forward in time using a fully explicit low-storage third-order Runge-Kutta scheme [27]. In the scheme, two storage locations are employed for each time-dependent variable and at each sub-step at these locations, say Q_1 and Q_2 with Q representing the solution variables, are updated simultaneously as follows

$$Q_1^{new} = a_1\ Q_1^{old}\Delta t + Q_2^{old}, \qquad Q_2^{new} = a_2\ Q_1^{old}\Delta t + Q_2^{old}. \tag{8}$$

The constants (a_1, a_2) in Eq. 8 were chosen to be (2/3, 1/4) for sub-step 1, (5/12, 3/20) for sub-step 2 and (3/5, 3/5) for sub-step 3. At the beginning of each full time step, Q_1 and Q_2 were set to be equal. The data in Q_1 was used to compute the time derivative terms of the solution variables. The computed time derivatives were stored in Q_1 to save storage (overwriting the old Q_1). Equation 8 was then used to update Q_1 and Q_2. In Eq. 8, Δt is the time step, which was limited by the Courant-Friedrichs-Lewy condition for stability and a chemical restraint [18].

3 Numerical Results and Discussion

3.1 The computational cases and input parameters

Several computational cases have been performed to investigate the effects of swirl and downstream wall confinement on the dynamics of the annular nonpremixed jet flame, as shown in Table 1. The five cases include two cases S0 and S0W without swirl, and three cases S04, S04W and S08 with swirl. Three cases S0, S04 and S08 are without downstream wall confinement, and two cases S0W and S04W are with downstream walls. In the simulations performed, the considered jet Mach number was $M = 0.4$, the Reynolds and Prandtl numbers used were $\mathrm{Re} = 2500$ and $\mathrm{Pr} = 1$. The nominal Reynolds number was based on the reference quantities defined in

Table 1 Summary of the computational cases

Computational cases	Case S0	Case S0W	Case S04	Case S04W	Case S08
Swirl number	0	0	0.4	0.4	0.8
Downstream wall confinement (yes/no)	N	Y	N	Y	N

the previous section. For a typical combustion application, these nondimensional parameters used correspond to a nozzle diameter of around 0.4 mm. However, test simulations showed that the results did not change appreciably if the Mach number was changed from 0.4 to 0.1 (lower Mach numbers led to much smaller time steps), indicating that the results can be representative for nozzle diameter up to 1.6 mm or even larger dimension, with injection velocity ranging approximately from 30 m/s to 120 m/s. It is important to note that DNS was mainly intended for better understandings of the physical problem, although scaling to larger configurations can be approximate or even distorted. It is also worth noting that the Reynolds number used is lower than that encountered in practical combustion applications. Increasing the Reynolds number would increase the requirements on computing resources significantly, which is beyond the affordability of this parametric computational study.

In the simulations, the ratio of specific heats used was $\gamma = 1.4$. The dynamic viscosity was chosen to be temperature-dependent according to $\mu = \mu_a (T/T_a)^{0.76}$. Parameters used in the one-step chemistry were: Damköhler number $Da = 6$, Zeldovich number $Ze = 12$, flame temperature $T_{fl} = 6$, and heat of combustion $Q_h = 150$, respectively. These values were chosen to give temperatures of a reacting flow typically encountered in many nonpremixed flames.

The dimensions of the computational box used were $L_x = L_y = L_z = 6.0$. A $256 \times 256 \times 256$ grid system with uniform distribution was used. For the three computational cases S0, S04 and S08 without downstream wall confinement, a sponge layer [17–19] was used in the downstream locations of $5.25 < z \leq 6.0$ to prevent the spurious waves from being reflected back into the domain from the outflow boundary. A grid independence test was performed and further refinement of the grid by doubling the points in each direction did not lead to appreciable changes in the instantaneous results. The time step was limited by the Courant-Friedrichs-Lewy condition for stability and a chemical restraint [18]. In the data analysis, the results for the sponge layers have been ignored since they are not truly physical. In the following, instantaneous results of the flow and combustion fields are presented and discussed first, followed by Fourier analysis of the velocity history and a proper orthogonal decomposition analysis of the instantaneous velocity field, and finally time-averaged results are presented and discussed.

3.2 Instantaneous flow results

Figures 1 and 2 show the instantaneous reaction rate contours in one cross-streamwise plane (mid-location $y = 3$ in the y-direction), and two streamwise planes including an upstream location $z = 1$ and the mid-location $z = 3$ after the flame has been developed, for the five cases investigated, respectively. The results indicate that the annular nonpremixed flame develops complex dynamic structures. From the reaction rate in the $y = 3$ plane, it is noticed that there is a flame located very close to the burner surface. This flame near the burner mouth can stabilize the combustion by providing a continuous and stable source of energy for ignition. The annular reacting flow also developed unsteady vortical structures, which are evident in the wrinkled flame structures in the jet columns. The vortical structures are caused by the Kelvin-Helmholtz type shear layer instability that can play a significant role in mixing and entrainment. In Figs. 1 and 2, it is observed that, under the swirling

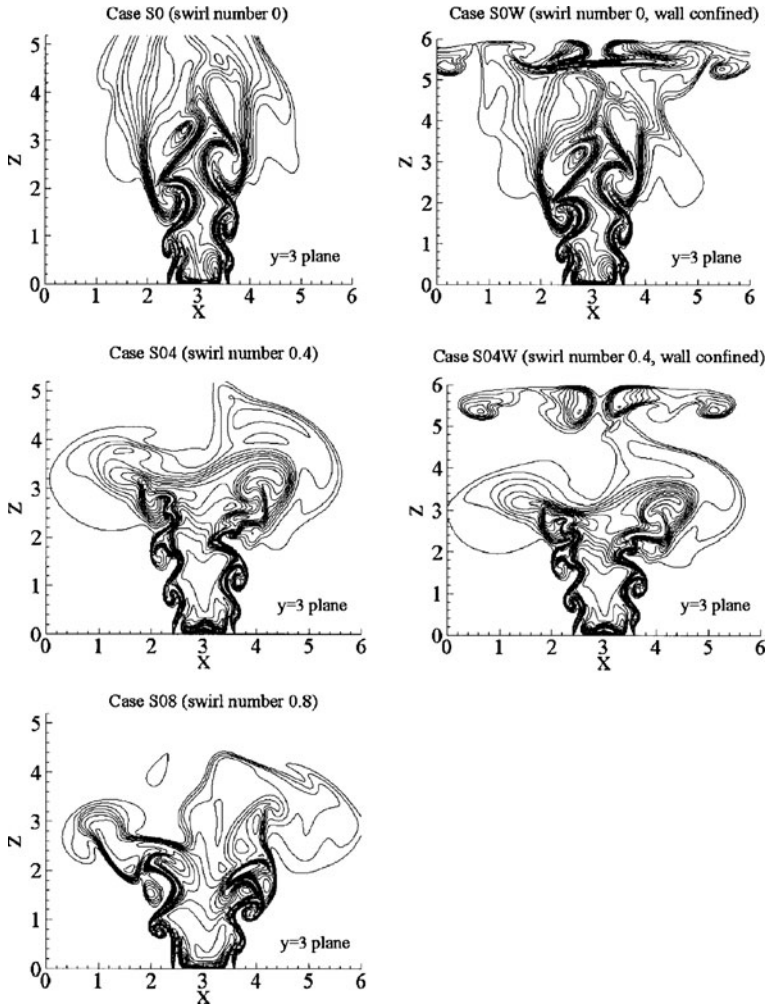

Fig. 1 Instantaneous reaction rate contours in the cross-streamwise section $y = 3$ at $t = 30$

conditions, the flame develops into a more spread structure and the flame without the downstream wall confinement becomes shorter. Swirl extends the curved shear layer and promotes mixing and combustion; therefore the flame becomes shorter and more spread.

The effects of downstream wall confinement can also be observed in Fig. 1. In the streamwise planes $z = 1$ and $z = 3$ in Fig. 2, there is not an appreciable difference between the corresponding cases with and without downstream wall confinement. In Fig. 1, there are reaction zones attached to the downstream walls in cases S0W and S04W due to the wall confinement. With the presence of the downstream wall, fuel and oxidizer can mix in the near-wall region to enable combustion. Consequently a near-wall flame can be established, associated with the formation of a wall jet due to the impingement. It is noticed that at this time instant there is almost no reaction at

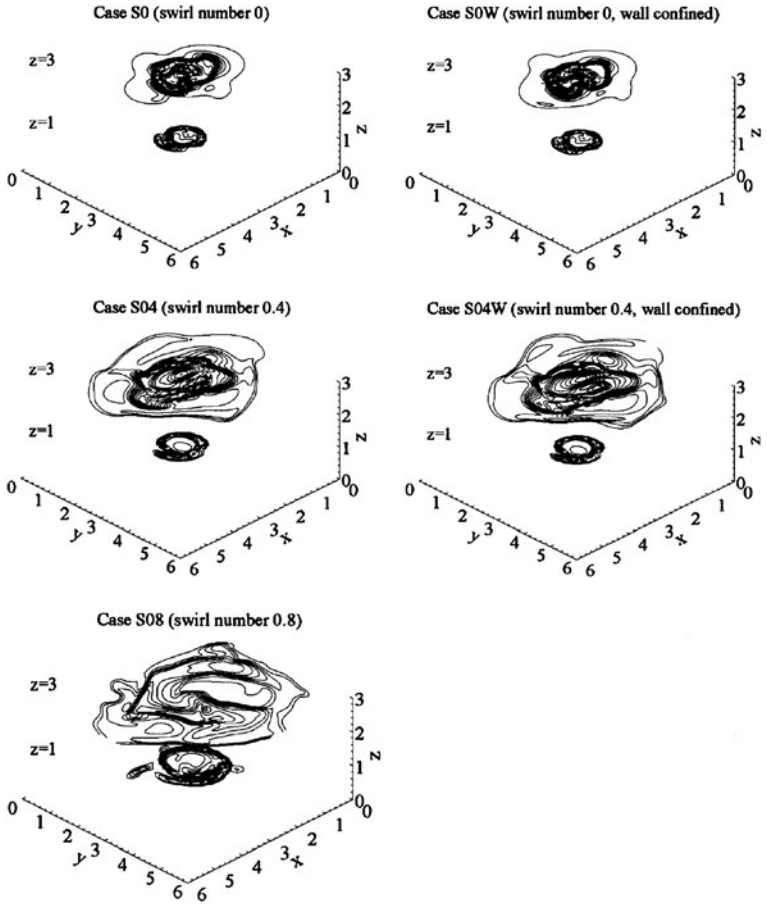

Fig. 2 Instantaneous reaction rate contours in the streamwise sections $z = 1$ and $z = 3$ at $t = 30$

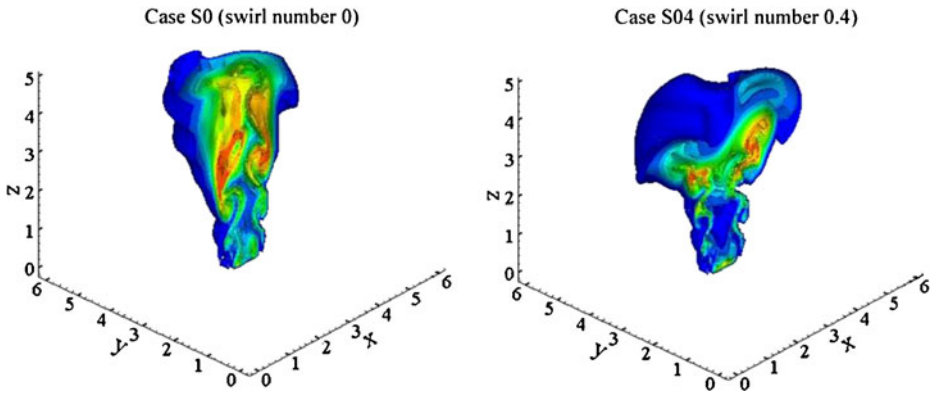

Fig. 3 Sample 3D instantaneous reaction rate isosurfaces (half-domain) at $t = 30$

around ($x = 3$, $y = 3$, $z = 6$), due to poor mixing between the fuel and oxidizer and strong normal strain in the stagnation zone at this location in the near-wall region. In Figs. 1 and 2, the asymmetry of the flame is due to the flapping modes, which is not spatially symmetrical about the centre of the domain.

To have an overall view of the flame, Fig. 3 shows sample 3D instantaneous reaction rate isosurfaces (half-domain), for the two non-impinging cases without swirl and with swirl number 0.4. In Fig. 3, it is observed that, under the swirling condition, the flame develops into a "mushroom" like structure and the flame becomes shorter but with larger spreading at the downstream locations. The results for the case with swirl number 0.8 and the other two impinging cases, which have not been shown for brevity, follow the same trends shown in Figs. 1 and 2.

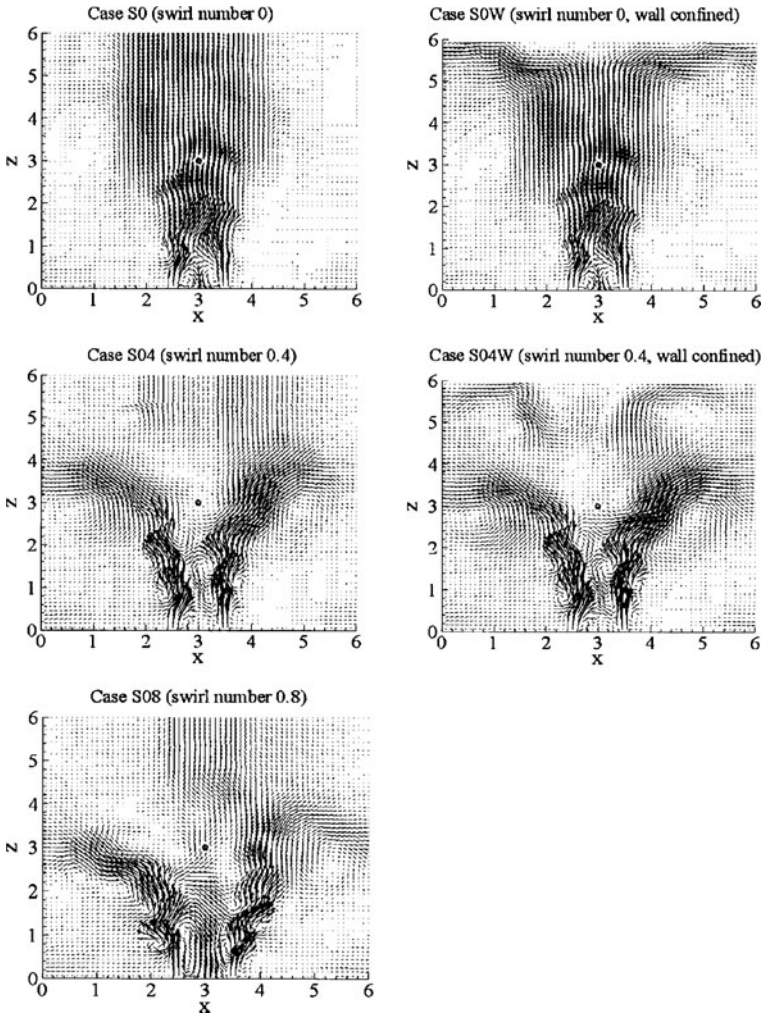

Fig. 4 Instantaneous velocity vector fields in the cross-streamwise section $y = 3$ at $t = 30$

Corresponding to the instantaneous reaction rate fields discussed above, Figs. 4 and 5 show the instantaneous velocity vector fields in the cross-streamwise plane $y = 3$ and streamwise plane $z = 3$ at $t = 30$, respectively. The vortical structures in the non-swirling cases are mainly associated with the development of Kelvin-Helmholtz instability, triggered by the flapping modes applied at the velocity inlet. In Fig. 5, the swirling cases show an anti-clockwise flow movement in the two streamwise planes, which is due to the swirling condition specified at the domain inlet. However, it is noticed in Fig. 5 that the centre of the anti-clockwise flow movement has moved away from the geometrical centre of ($x = 3$, $y = 3$) in the plane of $z = 3$, while it is roughly located at the geometrical centre in the upstream plane of $z = 1$. This indicates the formation of the swirl-induced PVC [28, 29], which is a well-known three-dimensional time-dependent instability caused by the swirling motion. For the non-swirling cases, the flow field in the streamwise cross-sections has

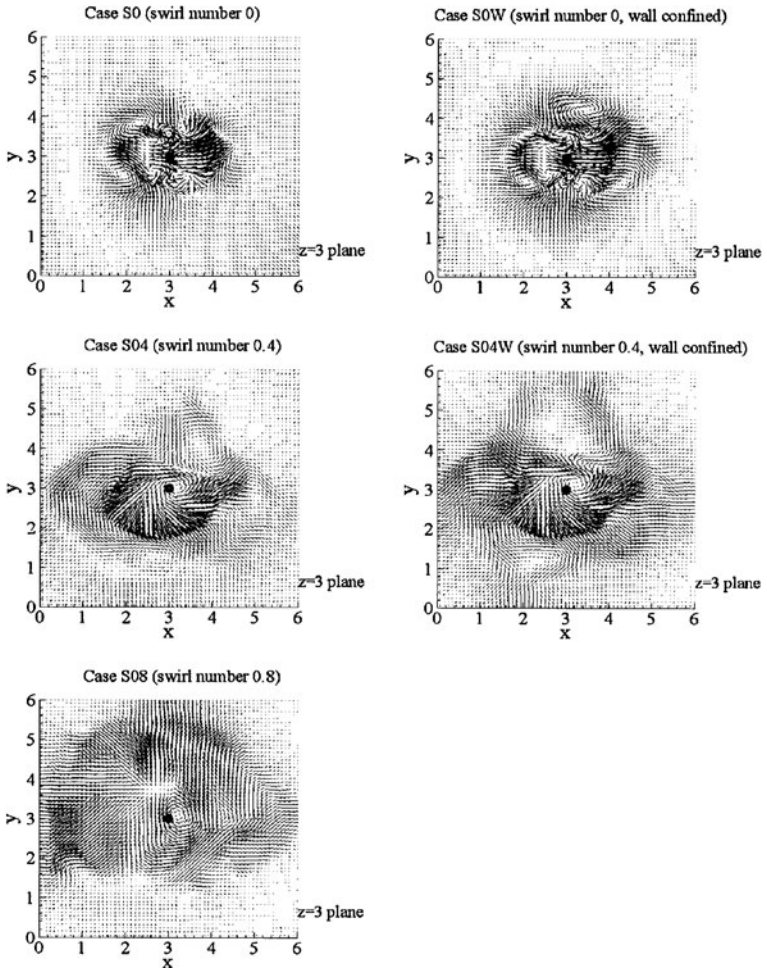

Fig. 5 Instantaneous velocity vector fields in the streamwise section $z = 3$ at $t = 30$

a complex structure due to the development of the shear layer instability triggered by the flapping modes in the small external perturbation provided at the nozzle exit. For the swirling cases, there are weak structures associated with the flapping modes around the rotating core. The flow fields of the swirling cases in the $z = 3$ plane indicate the existence of PVC, featuring the vortex core rotating associated with swirl. In Fig. 4, it can be observed that the impinging flows in cases S0W and S04W touch the downstream wall at the location of $z = 6$ with the formations of a stagnation zone in the impinging region and wall jets in the surrounding areas, which are more evident in the non-swirling case.

For impinging flames, the near wall heat transfer can be measured by the Nusselt number, which is a dimensionless number that measures the enhancement of heat transfer when convection takes place. It is defined as $Nu = hD/k$, where D is the jet nozzle diameter and k is the thermal conductivity of the fluid and h is the heat transfer coefficient defined as $h = -k\,(dT/dz)/(T_0 - T_w)$. Figure 6 shows the instantaneous Nusselt number at the wall in the $y = 3$ plane at $t = 30$ of cases S0W and S04W. In Fig. 6, it is evident that the distribution of the Nusselt number no longer has the well-known "bell shape" observed in round impinging jets [17, 24]. This is associated with the annular configuration of the flame, which has two branches in the cross section under investigation. The peak value of the Nusselt number of this annular flame is not far away from that observed in round impinging hot jets [17]. In Fig. 6, the asymmetry of the Nusselt number distribution is due to the flapping modes, which break the symmetry in the flow as shown in Figs. 1–5.

3.3 Fourier spectra and proper orthogonal decomposition results

In order to examine the interactions between the unsteady vortical structures, recirculation zones and the PVC associated with swirl, Fig. 7 shows the time traces of the temperature and streamwise velocity component at fixed points, which are one diameter and three diameters above the center of the nozzle exit. The corresponding Fourier spectra are shown in Fig. 8. As shown in Fig. 1, the point ($x = 3$, $y = 3$, $z = 1$) is on the inner side of the annular flame. At this upstream inner point, the flow is predominantly laminar and it becomes transitional downstream. From

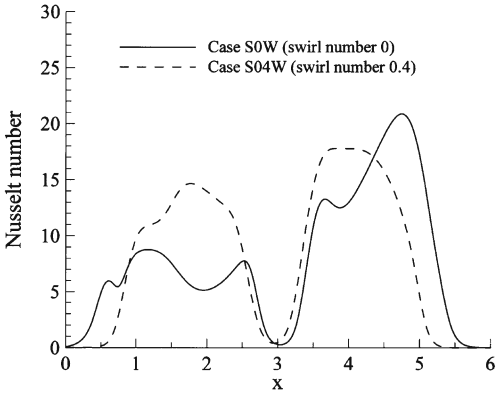

Fig. 6 Instantaneous Nusselt number at the wall in the $y = 3$ plane at $t = 30$ of cases S0W and S04W

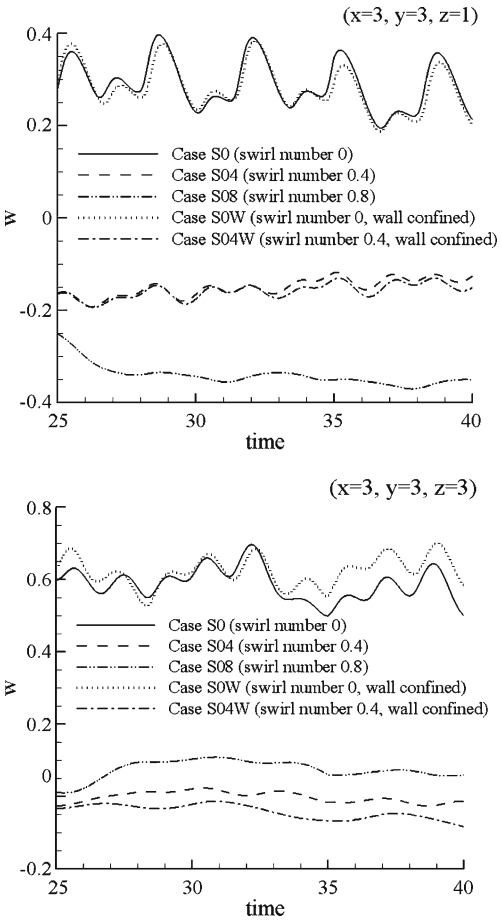

Fig. 7 Time traces of the streamwise velocities at ($x = 3$, $y = 3$, $z = 1$) and ($x = 3$, $y = 3$, $z = 3$)

Fig. 7, it is clear that the five cases behave quite differently, but the difference is small between the corresponding impinging and non-impinging cases, as the two points ($z = 1$ and 3) are still far from the wall. For the non-swirling cases, the streamwise velocities vary significantly and periodically, indicating that the flow field is dominated by the jet preferred mode of instability. The swirling cases do not show similar behaviour. Without swirl, the annular jet flow field is dominated by the unsteady vortical structures due to the Kelvin-Helmholtz instability. This instability is due to the existence of the two adjacent shear layers, which leads to the formation of vortical structures in the annular jet columns. Under swirling conditions, the vortical structures in the jet columns interact with the rotating inner structure. The presence of CRZ and PVC in the swirling cases changes the flow field of the annular jet flame significantly. In Fig. 7, it can be seen that the streamwise velocity at ($x = 3$, $y = 3$, $z = 1$) of the swirling cases is negative, indicating flow reversals. The flow reversals can promote the fuel/air mixing at upstream locations and increase the upstream temperature by bringing the hot combustion product backwards to regions near the burner mouth.

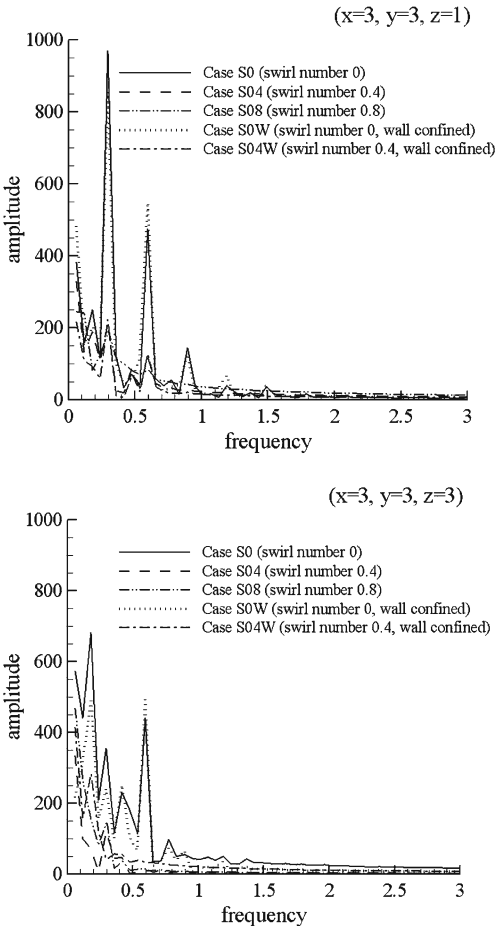

Fig. 8 Fourier spectra of the streamwise velocities at ($x = 3$, $y = 3$, $z = 1$) and ($x = 3$, $y = 3$, $z = 3$)

An important feature in Fig. 7 is that the reacting flow fields at ($x = 3$, $y = 3$, $z = 1$) and ($x = 3$, $y = 3$, $z = 3$) fluctuate significantly and periodically without swirl while the flow periodicity is almost diminishing for the swirling cases. The Fourier spectra shown in Fig. 8 can further clarify this. In Fig. 8, it can be seen that for the non-swirling cases the dominating frequency of the velocity is 0.30, with 0.60 as the second important frequency. The development of the frequency 0.60 is mainly associated with the fact that two flapping modes were superimposed, which not only broke the flow symmetry but also led to the development of the first super-harmonic frequency in the flow. At further downstream location of ($x = 3$, $y = 3$, $z = 3$), the frequency of 0.30 is no longer dominant, but the frequency of 0.60 is important. For the swirling cases, the flow does not have a non-zero dominating frequency because the flow does not develop into periodic behaviour. This is due to the fact that the vortical structures in the annular jet columns interact with the inner structures of the jet such as the swirl-induced large CRZ and PVC, characterized by flow reversals in the streamwise direction and rotating motions in the cross-streamwise direction. Unlike the dynamical vortical structures due to the Kelvin-Helmholtz type

shear layer instability, the inner structures associated with the CRZ do not change appreciably with time when the flow is developed; therefore the flow periodicity is diminishing.

Fourier transformation is based on one-point history data and there is no correlation with neighboring points. Therefore it may not reflect accurately the dynamics of the flow field. To overcome this weakness, a POD analysis was performed for the history data of the flow field. As a powerful tool to investigate the mode effects in vortical flow fields and turbulence, POD can be used to analyze the flow data generated by the DNS. The principle of POD is the decomposition of the flow field into a weighted linear sum of orthogonal eigenfunctions. The coherent structures in the flow field are described by the eigenfunctions of the two-point correlation tensor. The POD hypothesis is that different types of coherent motion that may occur within the flow will give rise to different POD eigenfunctions. The largest eigenvalue corresponds to the structure with most energy. The method of snapshots as described by Sirovich [30] was utilised in this work to solve the associated eigenvalue problem.

In this method, an ensemble of M discrete instantaneous flow variables (velocity fields in this study) acquired at time instants t_k, $k = 1, 2, ..., M$ is considered in a two-dimensional (2D) slice A of the 3D computational domain. The POD analysis is performed primarily in 2D slices cut in the streamwise and cross-streamwise directions to avoid the excessive computer memory requirements of a full 3D POD analysis of the DNS datasets. The full grid resolution of the DNS data is used. Firstly, the time-average of the velocity field is computed and the fluctuating velocity field $\xi(\vec{x}, t)$ is calculated. A two-point correlation matrix $\boldsymbol{C}$ is then constructed as $C_{i,j} = \int_A \xi(\vec{x}, t_i)\, \xi\left(\vec{x}, t_j\right) d\vec{x}/M$, where $i, j = 1, 2, ..., M$. The eigenvectors $\vec{a}_k^n$ and their corresponding eigenvalues λ_k are found from the numerical solution of the equation $\boldsymbol{C}\,\vec{a}_k^n = \lambda_k\,\vec{a}_k^n$, where $k, n = 1, 2, ..., M$. Using the eigenvectors $\vec{a}_k^n$ of matrix $\boldsymbol{C}$, the POD eigenfunctions $\phi^n(\vec{x})$ at mode n, which are optimal for the representation of the corresponding DNS data, can be linearly constructed by combining the fluctuating velocity as

$$\phi^n(\vec{x}) = \sum_{k=1}^{M} \vec{a}_k^n \xi(\vec{x}, t_k) \tag{9}$$

The POD eigenfunctions are orthogonal while the eigenvalues are positive ($\lambda_k \geq 0$) in descending order $\lambda_k > \lambda_{k+1}$, where $k = 1, 2, ..., M$. Each eigenvalue quantifies the kinetic energy of the flow field datasets. The average fluctuating energy in the datasets can be calculated by summing up all the eigenvalues, $E = \sum_{k=1}^{M} \lambda_k$. The POD eigenfunctions can then be used to reconstruct the fluctuating velocity fields as

$$\tilde{\xi}(\vec{x}, t) = \sum_{n=1}^{N} \vec{a}_k^n \phi^n(\vec{x}) \tag{10}$$

where N is the number of POD modes to be used for the reconstruction. Equation 10 is known as the "POD reconstruction formula". In general, the first few modes capture most of the energy of the flow as quantified by the λ_k values. In other words, it is sufficient to use $N \ll M$ for POD reconstruction of large datasets.

A POD analysis as described above was performed for the instantaneous velocity fields for the time interval between $t_1 = 30.00$ and $t_2 = 43.33$, where hundreds of

Table 2 Normalized eigenvalues and their cumulative contributions to the fluctuating energy in the $y = 3$ plane of case S0W

Mode	1	2	3	4	5	6	7	8	9	10
λ_k, u-component (%)	39.03	36.57	15.26	4.158	1.694	1.572	0.786	0.356	0.202	0.146
$\sum\lambda_k$, u-component (%)	39.03	75.60	90.86	95.02	96.71	98.28	99.07	99.42	99.63	99.77
λ_k, w-component (%)	38.19	26.74	20.07	7.886	2.488	2.155	1.271	0.456	0.263	0.196
$\sum\lambda_k$, w-component (%)	38.19	64.93	85.01	92.89	95.38	97.53	98.81	99.26	99.52	99.72

instantaneous flow "snapshots" were recorded and analyzed. Sample results are shown in Tables 2 and 3 and Figs. 9, 10 and 11 for the velocity fields in the middle plane of the domain $y = 3$ for the two impinging cases. These results from the POD analysis correspond to the last time instant $t_2 = 43.33$ since the POD reconstruction was carried out for this time instant. Tables 2 and 3 provide the normalised eigenvalues and their cumulative contributions to the fluctuating energy in the plane of $y = 3$ for the non-swirling and swirling impinging cases respectively. From Tables 2 and 3, it is clear that more than 95% of the total energy, which is the normal criterion used to judge the number of important modes in the flow field, can be captured in the first five POD modes in both computational cases, for both velocity components u and w. In the meantime, the first ten modes captures more than 99% of the total energy, with the rest of the modes contribute only a negligible amount of energy to the flow field. The trend of the mode effects is also shown in Figs. 9–11, indicating an overall picture of the POD modal energy distributions in the flow field.

Figure 9 shows the energy content of each POD mode and fluctuating energy of the POD modes for the two velocity components (u, w) for the non-swirling case in the $y = 3$ plane, while Fig. 10 shows those for the swirling case. In these figures, the "energy content" represents the contribution of an individual mode while the "fluctuating energy" represents the cumulative contributions of the relevant modes. From Figs. 9 and 10, it is clear that the first four POD modes contain most of the energy of the flow. It is also observed that there is no significant difference between the modal energy distributions of the u-component and w-component. This indicates that the flow is of a multi-dimensional nature. The formation of vortical structure due to the development of the Kelvin-Helmholtz instability in the flow field leads to a multi-dimensional flow field. There are several modes important to the energy distributions of the flow field, corresponding to the vortical flow field. The mode effects on the flow field are shown in Fig. 11.

POD analysis can be used to reconstruct the flow fields to illustrate the mode effects. Figure 11 shows such reconstructions. In Fig. 11, reconstructed velocity fields based on the first six most energetic POD modes are shown, in the section of $y = 3$

Table 3 Normalized eigenvalues and their cumulative contributions to the fluctuating energy in the $y = 3$ plane of case S04W

Mode	1	2	3	4	5	6	7	8	9	10
λ_k, u-component (%)	37.01	31.66	17.63	7.893	1.799	1.464	1.034	0.578	0.361	0.176
$\sum\lambda_k$, u-component (%)	37.01	68.67	86.30	94.19	95.99	97.46	98.49	99.07	99.43	99.61
λ_k, w-component (%)	35.78	27.69	19.57	10.14	2.483	1.644	1.224	0.641	0.340	0.156
$\sum\lambda_k$, w-component (%)	35.78	63.47	83.04	93.18	95.66	97.31	98.53	99.17	99.51	99.67

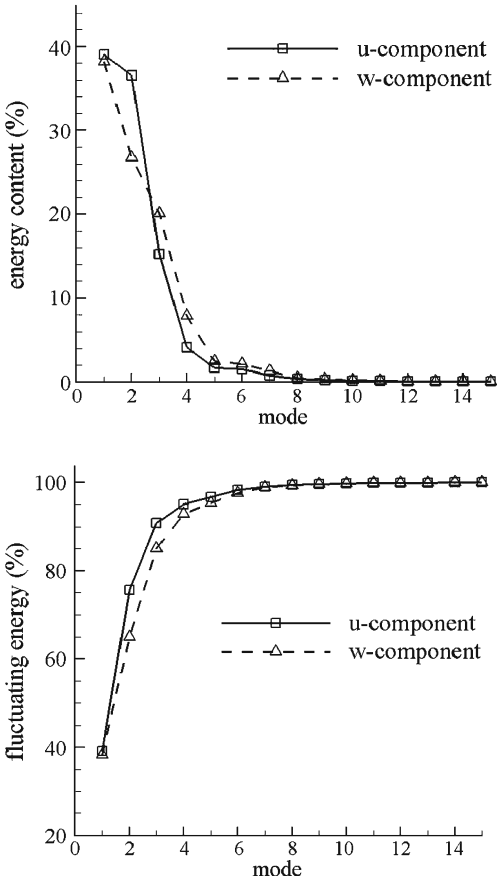

Fig. 9 Energy content of each POD mode and fluctuating energy of the POD modes for the two velocity components (u, w) in the $y = 3$ plane of case S0W

for the non-swirling impinging case. In this figure, it is evident that the flow field changes appreciably when the number of modes used in the velocity reconstruction is increased from 1 to 4, where the reconstructed flow field shows a gradual change with the increase of mode number. In the meantime, there is not any noticeable change when the number of modes used in the velocity reconstruction is increased from 4 to 6 with the reconstructed flow fields resembling the corresponding DNS fluctuating velocity field. The differences between the velocity fields reconstructed using different number of modes indicate the amount of energy captured by each mode. The modal effects are evident in the flow field reconstructed using different number of modes, showing the flow structural development. As the number of modes increases, the fluctuating energy captured increases and the reconstructed velocity field gradually approaches the DNS results. In Fig. 11, the most significant feature is that the wall effects are not captured when the number of modes used in the velocity reconstruction is small, indicating that the wall effects on the flow field are mainly associated with the higher mode numbers. The near-wall flow pattern is only reasonably captured when the total number of modes is increased to more than 3. The same trend was also observed for the swirling case. In this study, the POD analysis was performed in 2D slices to avoid the excessive requirements on computer

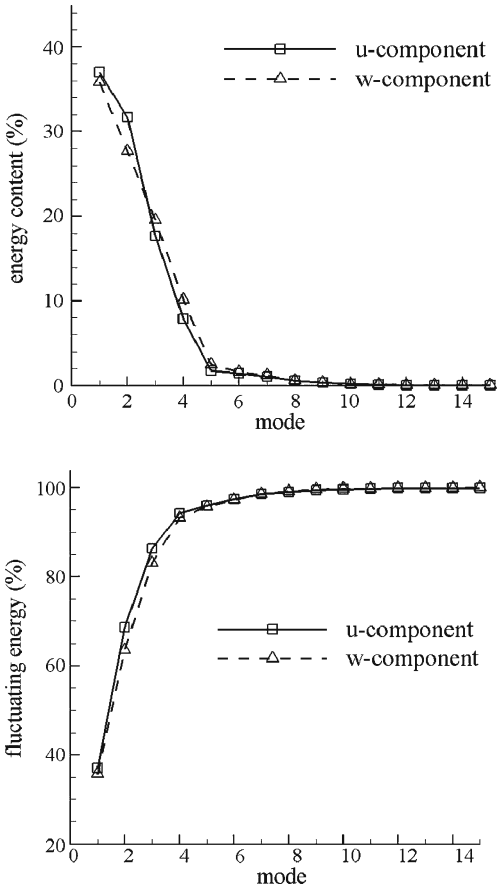

Fig. 10 Energy content of each POD mode and fluctuating energy of the POD modes for the two velocity components (u, w) in the $y = 3$ plane of case S04W

memory. A full 3D POD analysis of the DNS datasets would be required to achieve a finer analysis of the flow dynamics close to the wall.

3.4 Time-averaged flow results

Time averaging of the results was also performed to examine the mean flow properties and the effects of swirl and downstream wall confinement. The interval used for the averaging was $\Delta t : 30.00 \sim 43.33$, after the flow had reached a developed stage. The time interval chosen corresponds to four perturbation cycles as given in Eqs. 5–7. Figures 12 and 13 show the time-averaged flow and combustion properties along two lines in the middle plane $y = 3$ of the annular jet: the centreline $(x = 3, y = 3)$ in the stream direction and the line $(y = 3, z = 2)$ in the cross-stream direction. Figure 14 shows the streamwise velocity contours in this middle plane. In Figs. 12–14, it is evident that the time-averaged flow quantities remain asymmetric in this plane. This is because of the spatial asymmetry of the flapping modes applied at the domain inlet as indicated in Eqs. 5–7, which depend on the azimuthal angle regardless of the temporal variations or averaging. The helical perturbations were chosen because they lead to toroidal-like vortices often observed in laboratory flames, while the

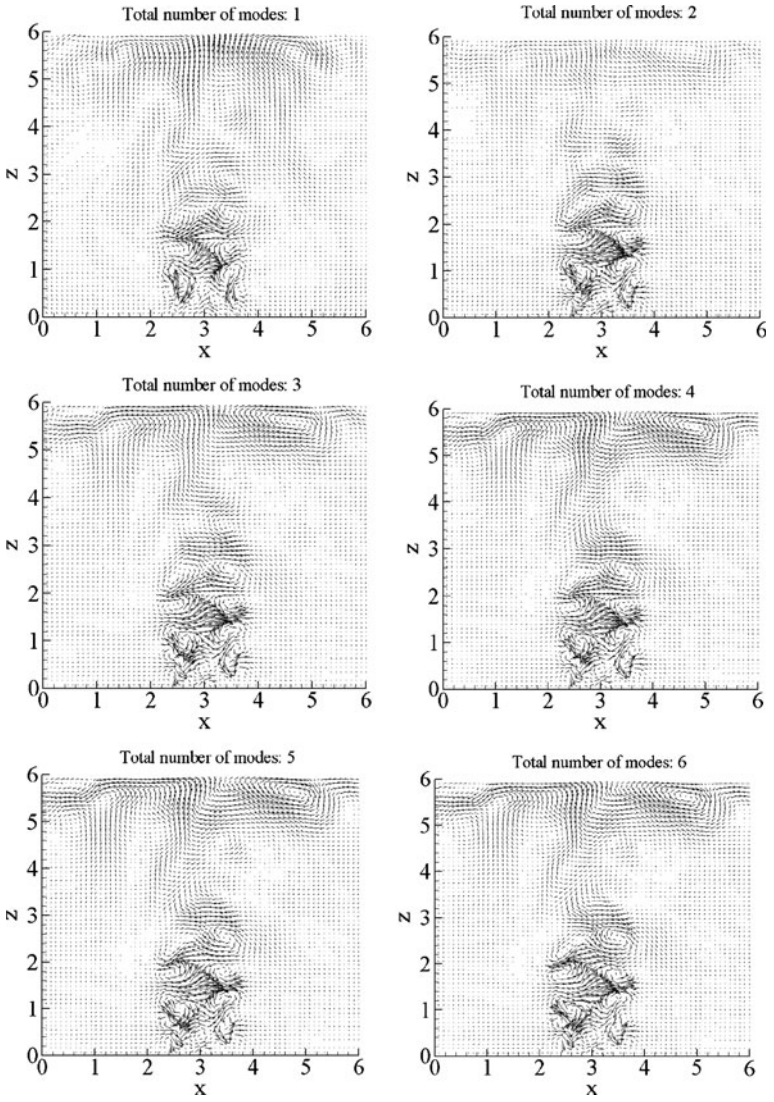

Fig. 11 Reconstructed velocity fields based on the first six most energetic POD modes in the $y = 3$ plane of case S0W

dependency of jet development on inlet disturbances has not been fully investigated in this study.

For the nonpremixed jet flame under investigation, the peaks observed in the averaged reaction rate profile correspond to locations where intense chemical reaction takes place when the fuel and oxidizer have been well mixed. In Fig. 12, it can be seen that the reaction rate profiles of all cases have at least two peaks along the jet centreline: a large one at downstream locations and a small one located very close to the burner mouth. The large peak at downstream locations corresponds to

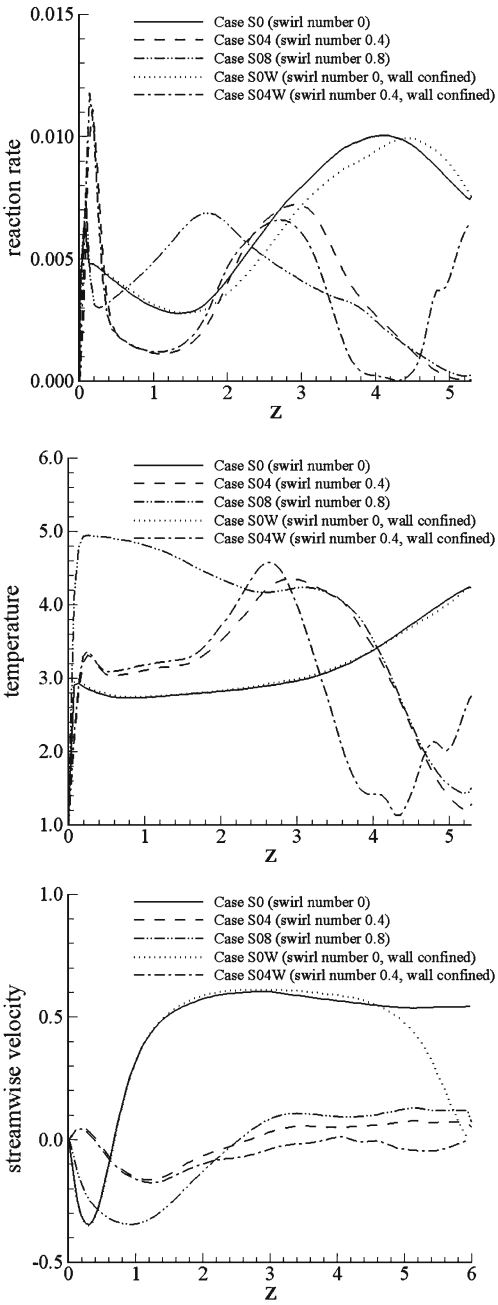

Fig. 12 Time-averaged reaction rate, temperature and streamwise velocity profiles along the centreline ($x = 3$, $y = 3$)

locations where intense chemical reaction takes place when the annular jet column has collapsed and the fuel and oxidizer have been well mixed. The small peak near the burner mouth is due to the formation of the GRZ inside the jet core. In an annular configuration, the existence of the GRZ adjacent to the nozzle exit is

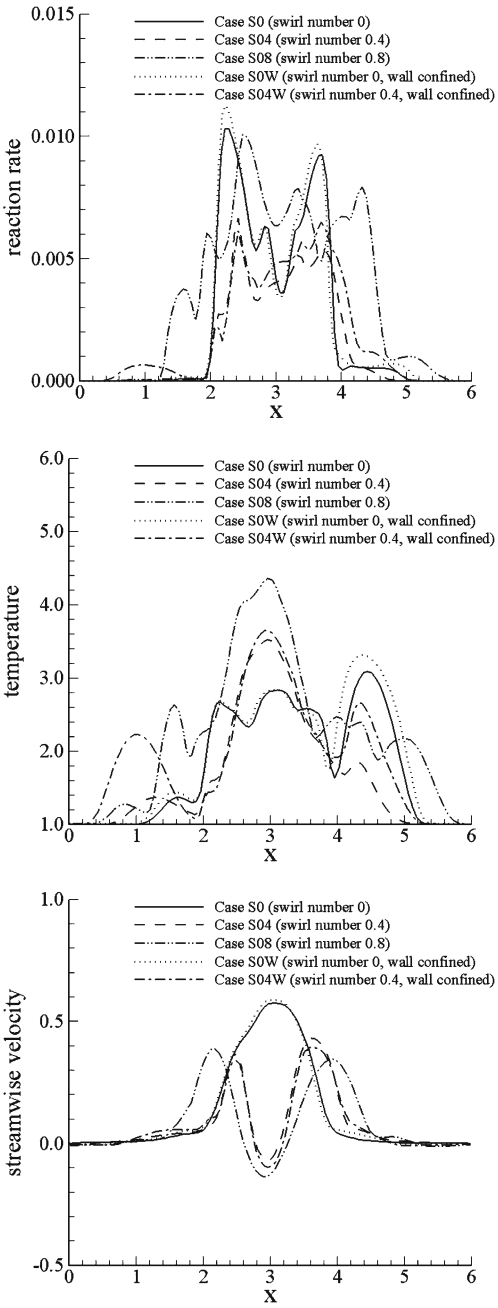

Fig. 13 Time-averaged reaction rate, temperature and streamwise velocity profiles along the line ($y = 3$, $z = 2$)

associated with the formation of a stagnation region when the jet column meets at the centre. The formation of this recirculation zone will bring the hot combustion product back to and enhance the fuel/oxidizer mixing near the burner mouth, thus leads to the formation of a flame attached to the burner mouth. It is observed

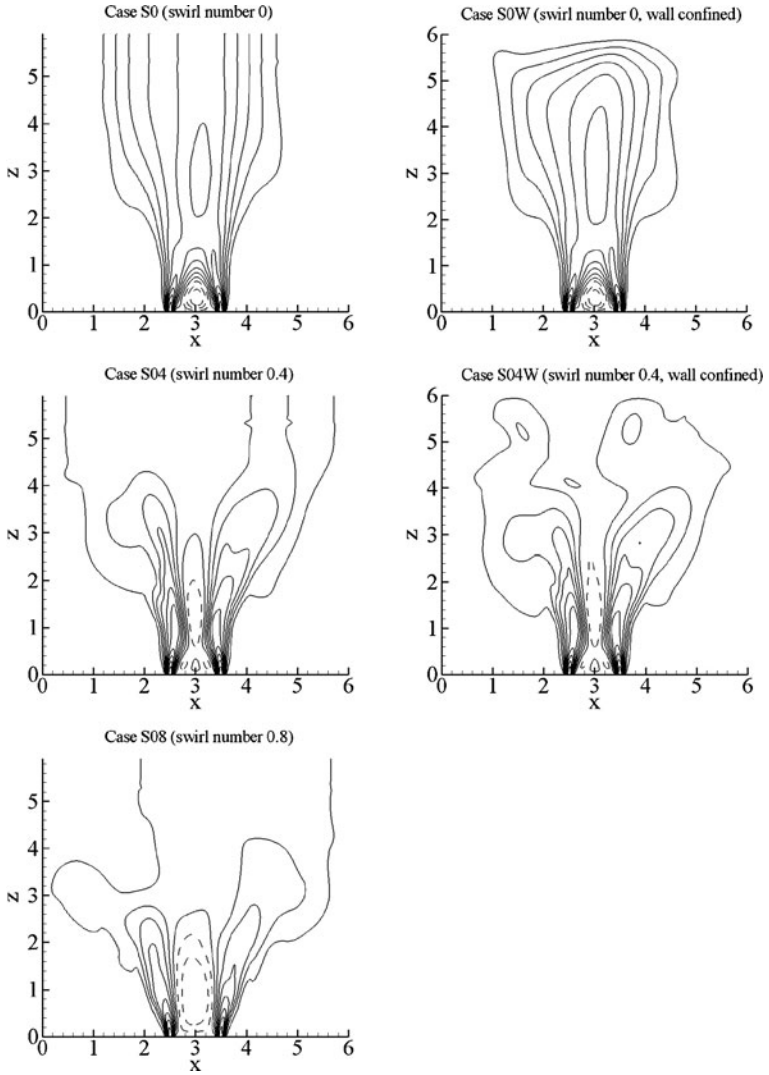

Fig. 14 Time-averaged streamwise velocity contours in the $y = 3$ plane (*solid line* positive, *dashed line* negative)

that the flame length reduces with the increase in swirl number, as shown in the averaged reaction rate along the jet centerline. This is because that swirl enhances the mixing between the fuel and oxidizer so that reaction is more complete at upstream locations.

In Fig. 12, it is observed that the downstream wall confinement does not affect the upstream flame appreciably. However, a near-wall reaction zone can be observed for the wall confined cases such as S04W, where the reaction rate has three peaks along the jet centerline due to the flame close to the burner mouth, the flame in the middle

of the domain when the annular fuel jet column collapse, and the near-wall flame due to the wall confinement. For the reaction rate of case S04W, there is a quenched region at the downstream location at around $z = 4$, where no significant reaction can be observed while above this location the formation of a reaction zone near the downstream wall can be observed. This is because of the enhanced fuel/oxidizer mixing associated with the wall impingement, which creates secondary shear layers associated with the wall jets. Consequently, the interactions between the annular configuration, swirling motion and wall impingement in this case led to several peaks in the averaged reaction rate profile along the jet centreline.

In Fig. 13, the profiles of reaction rate, temperature and streamwise velocity along the line $z = 2$ in the $y = 3$ plane show peaks and troughs associated with the effects of annular configuration and swirl. The asymmetric structure of the flame in this plane is evident in this graph. It is also clear that the temperature and reaction rate do not follow the same trend. The temperature of the reacting flow mainly depends on the local combustion heat release and the heat convection. In the annular swirling nonpremixed flame, the GRZ due to the annular configuration for the non-swirling cases is located very close to the nozzle exit, while the CRZ associated with swirl is located at slightly downstream locations in the swirling cases. Both the GRZ and the CRZ involve flow reversals, indicated by the negative streamwise velocity values in Figs. 12 and 13 and the dashed lines in Fig. 14. In the temperature profiles shown in Figs. 12 and 13, the high temperature regions correspond to regions with high reaction rate and small convective heat losses. In Fig. 12, it is noticed that the swirling cases do not have appreciable streamwise velocities at downstream locations after the CRZ. Between the two non-swirling cases, the flame without the wall confinement still has significant streamwise velocities at downstream locations near the far end of the computational domain due to the continuous development of the flame, while the streamwise velocity of the case with the wall confinement drops to a zero value at downstream locations near the far end of the domain.

The annular jet flame has a complex velocity field. The recirculation zone due to the annular configuration in the non-swirling cases is located very close to the nozzle exit, the CRZ of the swirling cases is located at slightly downstream locations, and the stagnation zone due to wall impingement in the two impinging cases are located further downstream. Under swirling conditions, the interaction between the recirculation zone due to the annular configuration and the swirl-induced CRZ significantly affects the flame dynamics. They are both located on the inner side of the jet column, involving flow reversals in proximity. Depending on the degree of swirl, the interaction leads to different consequences: they may co-exist or one zone may be overwhelmed by another. Figure 14 clearly displays this interaction. For swirl number 0.4, the "bell-shaped" recirculation zone GRZ and the CRZ co-exist, leading to a complex flow and an intensified reaction zone very close to the nozzle exit (indicated in Fig. 12) due to the enhanced mixing. As shown in Figs. 12 and 14, the interaction between and the co-existence of the GRZ and CRZ lead to a small positive streamwise velocity adjacent to the central point of the burn mouth. For swirl number 0.8, the results in Figs. 12 and 14 indicated that the GRZ has been overwhelmed by the CRZ due to the strong swirl in this case, where the "bell-shaped" GRZ completed vanished.

From the averaged flow quantities shown, it is noticed that the vortical structures in the jet column due to the Kelvin-Helmholtz type shear layer instability cannot be

observed. This is because that these structures are unsteady, which are continuously convected downstream by the mean flow and would not appear when the flow field is time averaged. The results shown indicate that swirl has significant effects on the fluid dynamics of the flame, because of the interaction between the recirculation zone near the jet nozzle exit and the CRZ associated with swirl. The annular nonpremixed flame develops complex structures, where a recirculation zone is formed near the nozzle exit due to the annular configuration that stabilizes the flame. Under swirling conditions, the annular jet also develops the CRZ involving flow reversals at slightly downstream locations. Unlike the vortical structures in the jet column which are highly unsteady, the recirculation zones do not change appreciably with time. At a moderate swirl number 0.4, the co-existence of the GRZ and CRZ leads to a flame with strong reaction attached to the burner mouth, while the GRZ can be overwhelmed by the CRZ under strong swirling conditions with swirl number 0.8.

4 Concluding Remarks

In this study, the dynamics of an annular nonpremixed flame has been numerically explored by solving the compressible Navier-Stokes equations using DNS. Effects of swirl and downstream wall confinement have been examined in a comparative study, including a non-swirling case and two swirling cases with swirl numbers 0.4 and 0.8 without downstream wall confinement, and a non-swirling case and swirling case with swirl number 0.4 with downstream wall confinement. Both instantaneous and time-averaged results have been presented. The results show that swirl has significant effects on the fluid dynamics of the flame, because of the interactions between the GRZ due to the shear instability, and the CRZ and PVC associated with swirl. The flow and flame dynamics are also strongly affected by the downstream wall confinement.

The annular nonpremixed flame develops complex structures. Unsteady vortical structures in the jet column due to the Kelvin-Helmholtz type shear layer instability originated from the two adjacent annular shear layers have been observed. Under swirling conditions, the annular jet flame also develops PVC involving rotating motion and CRZ on the inner side of the jet column. The vortical structures in the jet column are highly unsteady, while the GRZ and CRZ do not change appreciably with time. The GRZ formed near the nozzle exit due to the annular configuration can stabilize the flame. This study identified that the GRZ near the burner mouth and the CRZ associated with swirl may co-exist or the GRZ may be overwhelmed by the CRZ, depending on the degree of swirl. At a moderate swirl number, the co-existence of the GRZ and the CRZ leads to a flame with strong reaction attached to the burner mouth; while at a high swirl number, the CRZ dominates over the GRZ. It was found that swirl has significant effects on the flame dynamics. At a higher swirl number, the flame becomes shorter but with much larger spreading at the downstream locations. The DNS results have revealed that the annular configuration stabilizes the flame, while swirl enhances mixing and spreading of the flame and consequently shortens the flame length. The Nusselt number distribution at the wall of the impinging flames reflects the effects of the flow configuration. A POD analysis of the velocity field identified that the wall effects on the flow field are mainly associated with the higher mode numbers.

Finally, it should be noted that the present study is focused on the fluid dynamic aspects of combustion using correspondingly simplified one-step global reaction and transport properties. The incorporation of realistic chemical mechanisms and detailed transport is expected to add to a much richer picture of combustion physics, for example, autoignition, flame quench and re-ignition especially in the near-wall region. To simulate all these phenomena in a turbulent swirling impinging flame by a DNS would require orders of magnitude more computing resources. Yet the main features of flow–flame interactions through the GRZ, CRZ, PVC and wall impingement would remain the same, as the present annular swirling nonpremixed flame is mainly controlled by fluid dynamics and the mixing process.

Acknowledgements This work was supported by the UK EPSRC under Grant No. EP/G062714/1. The computing resources for this work were provided by the Consortium on Computational Combustion for Engineering Applications (COCCFEA) under EPSRC Grant No. EP/D080223/1 and the HPC-Europa Transnational Access programme. The authors also would like to thank Dr George Siamas for his input in the POD analysis.

References

1. Hübner, A.W., Tummers, M.J., Hanjalić, K., van der Meer, T.H.: Experiments on a rotating-pipe swirl burner. Exp. Therm. Fluid Sci. **27**, 481–489 (2003)
2. Masri, A.R., Pope, S.B., Dally, B.B.: Probability density function computations of a strongly swirling nonpremixed flame stabilized on a new burner. Proc. Combust. Inst. **28**, 123–131 (2000)
3. Masri, A.R., Kalt, P.A.M., Barlow, R.S.: The compositional structure of swirl-stabilised turbulent nonpremixed flames. Combust. Flame **137**, 1–37 (2004)
4. Jakirlić, S., Hanjalić, K., Tropea, C.: Modeling rotating and swirling turbulent flows: a perpetual challenge. AIAA J. **40**, 1984–1996 (2002)
5. Duwig, C., Fuchs, L.: Study of flame stabilization in a swirling combustor using a new flamelet formulation. Combust. Sci. Technol. **177**, 1485–1510 (2005)
6. Grinstein, F.F., Fureby, C.: LES studies of the flow in a swirl gas combustor. Proc. Combust. Inst. **30**, 1791–1798 (2005)
7. Sankaran, V., Menon, S.: LES of spray combustion in swirling flows. J. Turbul. **3**, Art. No. 011 (2002)
8. Selle, L., Benoit, L., Poinsot, T., Nicoud, F., Krebs, W.: Joint use of compressible large-eddy simulation and Helmholtz solvers for the analysis of rotating modes in an industrial swirled burner. Combust. Flame **145**, 194–205 (2006)
9. Stein, O., Kempf, A.M., Janicka, J.: LES of the Sydney swirl flame series: an initial investigation of the fluid dynamics. Combust. Sci. Technol. **179**, 173–189 (2007)
10. Kim, S.H., Pitsch, H.: Mixing characteristics and structure of a turbulent jet diffusion flame stabilized on a bluff-body. Phys. Fluids **18**, 075103/1–13 (2006)
11. Patte-Rouland, B., Lalizel, G., Moreau, J., Rouland, E.: Flow analysis of an annular jet by particle image velocimetry and proper orthogonal decomposition. Meas. Sci. Technol. **12**, 1404–1412 (2001)
12. Vanoverberghe, K.P., van den Bulck, E.V., Tummers, M.J.: Confined annular swirling jet combustion. Combust. Sci. Technol. **175**, 545–578 (2003)
13. García-Villalba, M., Fröhlich, J.: LES of a free annular swirling jet—dependence of coherent structures on a pilot jet and the level of swirl. Int. J. Heat Fluid Flow **27**, 911–923 (2006)
14. García-Villalba, M., Fröhlich, J., Rodi, W.: Identification and analysis of coherent structures in the near field of a turbulent unconfined annular swirling jet using large eddy simulation. Phys. Fluids **18**, 055103/1–17 (2006)
15. Al-Abdeli, Y.M., Masri, A.R.: Turbulent swirling natural gas flames: stability characteristics, unsteady behavior and vortex breakdown. Combust. Sci. Technol. **179**, 207–225 (2007)
16. Zhang, Y., Bray, K.N.C.: Characterization of impinging jet flames. Combust. Flame **116**, 671–674 (1999)

17. Jiang, X., Zhao, H., Luo, K.H.: Direct numerical simulation of a non-premixed impinging jet flame. ASME J. Heat Transfer **129**, 951–957 (2007)
18. Jiang, X., Luo, K.H.: Dynamics and structure of transitional buoyant jet diffusion flames with sidewall effects. Combust. Flame **133**, 29–45 (2003)
19. Jiang, X., Luo, K.H.: Mixing and entrainment of transitional non-circular buoyant reactive plumes. Flow Turbul. Combust. **67**, 57–79 (2001)
20. Poinsot, T.J., Lele, S.K.: Boundary-conditions for direct simulations of compressible viscous flows. J. Comput. Phys. **101**, 104–129 (1992)
21. Jiang, X., Siamas, G.A., Wrobel, L.C.: Analytical equilibrium swirling inflow conditions for computational fluid dynamics. AIAA J. **46**, 1015–1018 (2008)
22. Danaila, I., Boersma, B.J.: Direct numerical simulation of bifurcating jets. Phys. Fluids **12**, 1255–1257 (2000)
23. Uchiyama, T.: Three-dimensional vortex simulation of bubble dispersion in excited round jet. Chem. Eng. Sci. **59**, 1403–1413 (2004)
24. Jiang, X., Zhao, H., Luo, K.H.: Direct computation of perturbed impinging hot jets. Comput. Fluids **36**, 259–272 (2007)
25. Hussain, K.M.F., Zaman, K.B.M.Q.: The preferred mode of the axisymmetric jet. J. Fluid Mech. **110**, 39–71 (1981)
26. Lele, S.K.: Compact finite-difference schemes with spectral like resolution. J. Comput. Phys. **103**, 16–42 (1992)
27. Williamson, J.H.: Low-storage Runge-Kutta schemes. J. Comput. Phys. **35**, 48–56 (1980)
28. Syred, N.: A review of oscillation mechanisms and the role of the precessing vortex core (PVC) in swirl combustion systems. Pror. Energy Combust. Sci. **32**, 93–161 (2006)
29. Al-Abdeli, Y.M., Masri, A.R.: Precession and recirculation in turbulent swirling isothermal jets. Combust. Sci. Technol. **176**, 645–665 (2004)
30. Sirovich, L.: Turbulence and the dynamics of coherent structures. 1. Coherent structures. Q. Appl. Math. **45**, 561–571 (1987)